Science and Technology Indonesia
e-ISSN:2580-4391 *p*-ISSN:2580-4405
Vol. 9, No. 1, January 2024

Research Paper

Numerical Study of Early Detection of Tuberculosis Infected with High Sensitivity Plasmonic Sensor

Dedi Irawan[1*], Azhar[1], Khaikal Ramadhan[2], Azwir Marwin[3], Arip Marwan[4]

[1]*Department of Physics Education, Faculty of Teacher Training and Education, Riau University, Pekanbaru, 28293, Indonesia*
[2]*Department of Physics, Faculty of Mathematics and Natural Science, Bandung Institute of Technology, Bandung, 40132, Indonesia*
[3]*Department of Physics, Faculty of Mathematics and Natural Science, Riau University, Pekanbaru, 28293, Indonesia*
[4]*Department of Electrical Engineering, Faculty of Engineering, Riau University, Pekanbaru, 28293, Indonesia*
***Corresponding author**: dedi.irawan@lecturer.unri.ac.id

Abstract
In this work, a photonic crystal fiber based on a plasmonic sensor for the early detection of tuberculosis has been designed with finite element analysis. The component is constructed with a substrate layer made of fused silica material, which is then coated with a thin film of TiO_2 layer as an adhesive layer to strongly attach the Au layer with the silica fiber surface. The TiO_2 layer has an optimal thickness of 45 nm, while the Au layer has a thickness of 50 nm. The sensor design has a refractive index (RI) detection range from 1.27 RIU to 1.37 RIU, it also shows a maximum wavelength sensitivity (WS), maximum amplitude sensitivity (AS), sensor resolution (SR), and sensor accuracy (SA) of 20,000 nm/RIU (x-polarized) and 17.000 nm/RIU(y-polarized), -211.38 1/RIU (x-polarized) and -211.211 1/RIU (y-polarized), 9.17×10^{-5} RIU (x-polarized) and 1×10^{-4} RIU (y-polarized), and 0.025/nm respectively. Tuberculosis exhibits a normal and infected RI range of 1.343 RIU to 1.351 RIU. Therefore, the proposed sensor design is capable of detecting four types of TB infections with high sensitivity.

Keywords
Sensor, Photonic Crystal Fiber, Plasmonics, Tuberculosis Detection

Received: 30 June 2023, Accepted: 4 December 2023
https://doi.org/10.26554/sti.2024.9.1.94-102

1. INTRODUCTION

Tuberculosis is a deadly disease caused by mycobacterium bacteria that has infected many people almost everywhere in the world, according to WHO data from 2022, more than a million people have been infected with this disease so far (Geneva, 2023). Tuberculosis kills 1.5 million people every year and makes it the main cause of death in the world, this requires good management by all parties to prevent more victims from falling. WHO estimates that in 2020 this disease will be the number two cause of death. In line with the Covid 19 pandemic that has hit people all over the world, it is estimated that patients who test positive for Covid-19 and then contract tuberculosis will have a high death rate in 2022. Finally, significant ongoing efforts must be made to design, test, and, build systems where possible before shipping them to the medical field. Furthermore, efforts to meet early detection mechanisms will yield interesting and useful results. In general, detection techniques must meet a number of criteria, high accuracy and low operating loss are a few examples, of portable devices, and fast response speed. Optical components are expected to meet the requirements and be a solution in the early detection of tuberculosis. Early detection will also have a significant impact on the health care system so that tuberculosis cases can be prevented and action can be taken quickly to reduce the number of lives lost.

The optical component is a component that works on wavelength, it requires light energy to define the sensor signal, and because light has a very high speed, it allows this component to perform very fast sensing when compared to electron-based components. To be used as a sensor, sophisticated fabrication technology is required, as well as relatively higher costs, whereas the developments produced by this component are very rapid by utilizing numerical methods to determine sensor capabilities without the need to fabricate and combine as a system. The finite element method is a popular method among researchers for demonstrating and characterizing sensor performance. Fiber Bragg grating (FBG), SMF, MM, MZI, PHC, PCF, and PCF-SPR are examples of optical components that have shown promise in medical applications thus far (Irawan et al., 2022a; Tosi et al., 2018; Zaki et al., 2022; Panda and Pukhrambam, 2022; Li et al., 2022; Abdelghaffar et al., 2022;

Kumar et al., 2023; Otupiri et al., 2015).

Plasmonic sensor with Photonic crystal fibers (PCF) have been extensively studied using numerical simulation (Irawan et al., 2022c; Irawan et al., 2022b; Gu et al., 2022), the loss experienced by this component is advantageous for application in many fields such as, in the industrial, biomedical, chemical engineering, food, and environmental fields (Kumar et al., 2023; Chen et al., 2023; Sarker and Faisal, 2023; Kumar et al., 2023) . This component is highly recommended for measuring physical quantities such as temperature, strain, refractive index (RI), and magnetic field due to its extremely high sensitivity when compared to conventional fiber optic components (Han et al., 2019; Wu et al., 2021). When PCF is combined with a metal layer, an electron resonance event occurs that is extremely sensitive to environmental disturbances. Air holes in the PCF core are also used to allow analytes into the sensor, allowing it to have micro-component sizes, during development, the sensor components in analyte sensing are divided into external sensing and internal sensing; in external sensing, the Au layer is placed on the component's outer layer, whereas, in internal sensing, the Au layer is located on the sensor core. This component has been developed specifically in the medical world for the early detection of several diseases, such as the early detection of skin cancer cells (Eid et al., 2021; Irawan et al., 2022d), breast cancer, liver cancer, blood cancer, and early detection of cholesterol (Ramola et al., 2021; Jabin et al., 2019; Rahaman et al., 2022; Kumar et al., 2023), and we conducted a numerical study for this sensor component in the early detection of tuberculosis in this work. The difference in RI between disease-infected and healthy cells serves as the reference for PCF-based sensing (Pan et al., 2022), because this component is ultra-sensitive, it will excel at diagnosing diseases based on the RI (Shakya and Singh, 2022).

Many researchers have worked on the development of optical-based tuberculosis sensors, several optical components have been reported to be capable of correctly detecting normal cells and tuberculosis-infected cells, the proposed sensor components are made of TiO_2 and SiO_2 materials and have a WS of 700 nm/RIU (Ramanujam et al., 2020). In 2021, Taya et al. (2021) developed a photonic crystal-based nano-sensor to detect tuberculosis bacteria, which was based on numerical simulations using the TM method, the sensor is made of BaF_2 and GaAs materials, and it has a max sensitivity of 3197.18 nm/RIU. A tuberculosis biosensor based on band gap material was proposed by Aly et al. (2021), in the his design, it achieved a sensitivity of up to 1390 nm/RIU, and the materials used in the sensor simulation were TIN and TiO_2. In 2023, Mohammed et al. (2023) performed numerical simulations for photonic crystal sensor components in detecting tuberculosis, the proposed components were made of ZEONEX material and it had a wheel-shaped sensor geometry structure, a sensor sensitivity of 90.6%, an effective area component of $4{,}342 \times 10^{-8}$, and a confinement loss of 3.13×10^{-9} 1/cm were obtained after numerical analysis. During the same year, Parmar et al proposed a RI-based graphene sensor with a sensitivity of 1000 nm/RIU for detecting Mycobacterium tuberculosis (Parmar et al., 2022). The researcher's previous sensor proposal still has low sensitivity and should be improved by using a combined PCF and SPR sensor component. Based on the RI, we propose a highly sensitive optical component for the early detection of tuberculosis-infected cells in this paper.

2. EXPERIMENTAL SECTION

2.1 Method

In this study, we used SiO_2 dielectric material as the background component material, and TiO_2 material to connect the dielectric and plasmonic materials and also simulate using the finite element method (FEM). All of these materials are defined numerically by using Equation 1 for silica, Equation 2 for Au, and Equation 3 for TiO_2. The sensing scheme proposed for this component is external sensing, in which the analyte is located outside the sensor layer and not in the core or cladding. Some of the parameters in the sensor geometry structure are d1 = 0.4 µm, d2 = 0.64 µm, and d3 = 0.8 µm, whereas analyte size, Au thickness, TiO_2 thickness, and PML thickness are 45 nm, 50 nm, and 1 µm.

Figure 1 depicts the sensor geometry structure in this section, many good geometric structures in detecting the RI have been reported by researchers, some of which have achieved good performance in several parameters, such as achieving components with very low loss, a very low loss geometry structure. The sensor geometry structure is simple to fabricate and has a high sensitivity. Despite the fact that research fabrication technology for this sensor component is still lacking, various types of PCF geometric structures have been reported, including hexagonal-shaped PCF, decagonal-shaped PCF, D-shaped PCF, and many more (Falah et al., 2022). Other factors, such as the type of air holes around the core, have been widely reported in addition to the sensor geometry structure. According to some sources, circular air holes have more advantages than hexagonal and spiral air holes. In designing the shape of the air holes in the core, the tendency of light to pass through the component core is also an important consideration (Irawan et al., 2022a; Irawan et al., 2022c).

In addition to the performance of other important things such as materials that are easy to find on the market and materials that make it easy to fabricate, the dielectric or metal constituent materials used in sensor components have a significant influence on sensor performance. Among the many background materials in sensors, fused silica material remains a very viable background material and has been tested for its ability and durability in commercial optical components, as reported by many previous researchers such as ZEONEX, TOPAS, and silica. Coatings on sensors, as well as external and internal sensing schemes, are other parameters to consider on sensors. For example, in this recent study, the researchers attempted to coat the sensor components with MXENE material, in addition to coating with TiO_2 material, to facilitate coating of silica with Au as a plasmonic material (Rahman et al., 2020; Sen et al.,

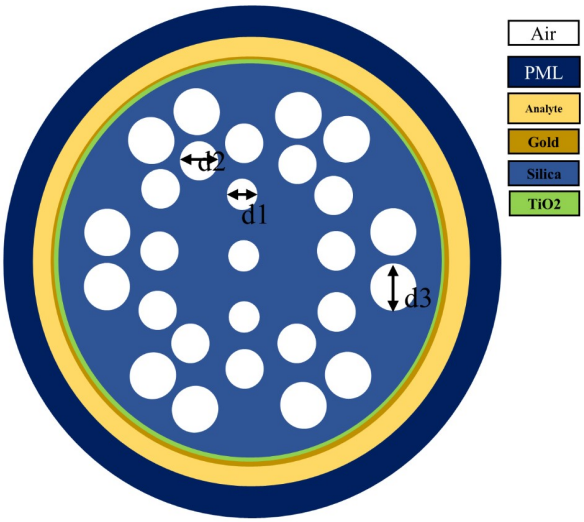

Figure 1. Optical Based Sensor System Sensor Geometry Structure with Three Types of Air Hole Sizes Around Different Cross Sections Each with Size d1 = 0.4 µm, d2= 0.64 µm, d3= 0.8 µm in this Component the Sensor is Composed of Silica, TiO_2 Material with a Thickness of d_{TiO_2} = 50 nm, Au with a Thickness of d_{Au} = 45 nm, and PML Which is the Limit of the Spread of Electromagnetic Waves Around the Sensor Cross Section

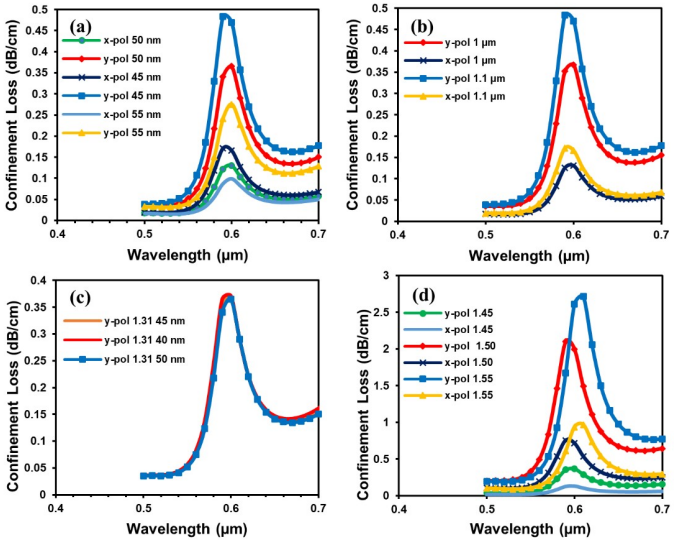

Figure 2. Confinement Loss Obtained from the Sensor Component Based on the Thickness of the Component Constituent Material, In this Case the RI of the Analyte is Set Equal to the Value of 1.31 RIU (A) the Thickness Variation of TiO_2, In this Case the Thickness of Tio_2 is Varied 40, 45, and 50 Nm, It is Obtained that for Each Polarization the X and Y Polarizations Experienced Significant Changes While the Thickness of the Material Did Not Show Significant Changes (B) Variations in Au Thickness, With Thicknesses of 45, 50, and 55 Nm Respectively, It Was Found that Au Thickness Affected CL Meanwhile Does Not Experience A RW Shift (C) Variations in Air Hole Diameter from 1.45 Um, 1.5 Um and 1.55 Um, a Wavelength Shift Occurs For Each Additional Air Hole Diameter, (D) Variations in PML Thickness From 1 Um and 1.1 Um For Each Polarization on X and Polarized on Y

2021; Kumar et al., 2023; Rifat et al., 2015; Yan et al., 2020; Liu et al., 2020).

2.2 Numerical Analysis

The SiO_2 refractive index defined from the Sellmeier equation in Equation 1 (Brixner, 1967), although ZBLAN material has a relatively better sensitivity than silica for a larger wavelength range, in this study we used silica material as the background material because for a shorter wavelength range it has a relatively good sensitivity than ZBLAN material and crown glass (Sellmeier, 1871).

$$n(\lambda) = \sqrt{1 + \frac{0.696\lambda^2}{\lambda^2 - 0.0047} + \frac{0.408\lambda^2}{\lambda^2 - 0.0014} + \frac{0.897\lambda^2}{\lambda^9 7.934}} \quad (1)$$

The plasmonic material used in this sensor is Au, as previously stated, the Au layer's dielectric constant is measured using the Drude Lorentz formula, and the dispersion is calculated based the wavelength of this formula. Table 1 describes the parameters in Equation 2 (Sehmi et al., 2017), although the sensitivity obtained by Au material is lower than silver material, chemically Au material is more stable than other metal materials, so in this study we used a thin layer of Au (Johnson and Christy, 1972).

$$\varepsilon_{au} = \varepsilon_{\infty} - \frac{\omega^2 D}{\omega(\omega + jyD)} - \frac{\Delta\varepsilon\Omega_L^2}{(\omega 2 - \Omega_L^2) + j\Gamma_L\omega} \quad (2)$$

$$n_{TiO_2} = \sqrt{E + \frac{F}{\lambda^{\alpha} - C}} \quad (3)$$

TiO_2 has a refractive index that leads to the release of numerous surface electrons, pulling to the plane of the core aids in interactions with the SPP mode, thus it is utilized as an adhesive layer between Au and SiO_2, and Equation 3 can help determine TiO_2's refractive index (Singh and Prajapati, 2020). Where n_{TiO_2} = RI of TiO_2, E= 5.193, F=2.441, and λ is in µm, The FE method is used in the PCF sensor structure to measure sensing performance using COMSOL Multiphysics, the variation of peak of the Confinement Loss (CL) spectrum in evaluating the sensitivity wavelength (WS) of the PCF sensor. Equation 4 can be used to calculate the characteristics of the CL curve for changes in refractive index (Matsui et al., 2005).

$$L_c(dB/cm) = \left(\frac{4\Pi f}{c}\right) Im(n_{eff}) \times 10^4 \quad (4)$$

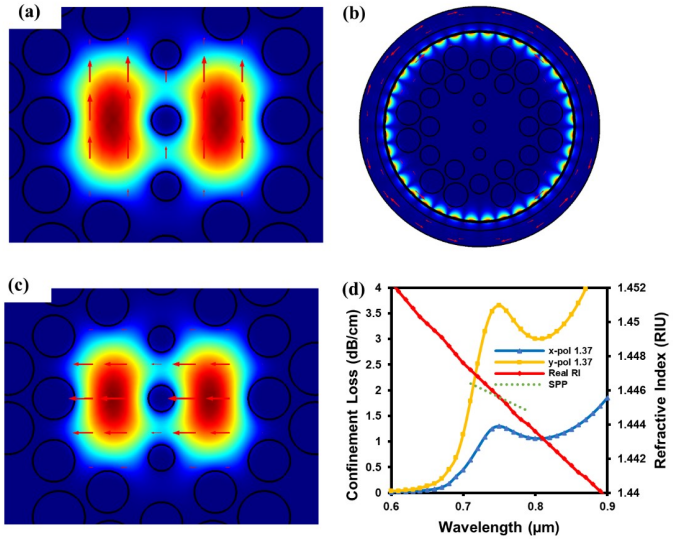

Figure 3. TE Mode Around the Dual-Core Sensor at Y Polarization, the RI of the Analyte in this Condition Is 1.36 RIU, (B) the SPP Mode on the Cross-Section of the Sensor Around the Au Layer Occurs an Electron Oscillation Phenomenon (C) TE Mode Around Dual-Core Sensor at X Polarization, in this Case The Refractive Index of the Analyte Is 1.36 RIU and (D) the Confinement Loss Graph at X Polarization, Y Polarization, Real RI and RI Of SPP Mode

Table 1. Value of Drude-Lorentz Equation

Symbols	Definition	Value
ε_{au}	permittivity value of Au	5.9673
ω	plasma frequency	2Π/0.75 μm
γ_D	dumping frequency	31.84Π THz
ω_D	plasmon frequency	4227.2Π THz
Ω_L	oscillator power	1300.14Π THz
Γ_L	Spectral width	209.72Π THz

Where Lc same as CL of the PCF, f is frequency, n_eff is the effective refractive index, and c is the light speed. Futuremore, the most important parameter of the PCF-SPR sensor are WS and Amplitude sensitivity (AS). The sensor sensitivity could be measured by using the wavelength and amplitude interrogation method. The Amplitude sensitivity is also a powerful technique which can be used in optical component based on the difference CL. The sensor with high sensitivity is needed in many sensor applications, especially in detecting tuberculosis in term on the refractive index of each type of tuberculosis and the refractive index of normal (uninfected) blood. Table 2 shows the refractive index of each type of tuberculosis-infected cell and normal cell (Mohammed et al., 2023). The external sensing introduced in this work allows tuberculosis samples not to be inserted into the air holes in the sensor components, while the sensing process only requires a medium or source

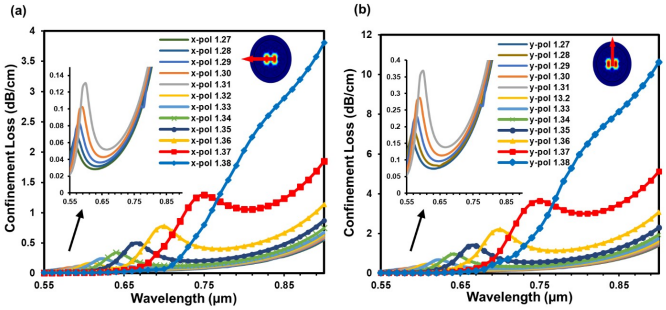

Figure 4. WS of the PCF-SPR Sensor Component with a Variation of Refractive Index From 1.27 RIU To 1.37 RIU, in These Conditions the Diameter of Au Dau = 50 Nm, Diameter Of TiO_2 $DTiO_2$ = 45 Nm, and Thickness Of PML = 1um, WS Shifts With Increasing the Refractive Index of the Analyte, and Also the RW Shifts with Each Increase in RI of the Analyte (A) Polarization on the X-Axis (B) Polarization on the Y-Axis

to avoid other environmental disturbances that may interfere with the sensor system.

Table 2. Refractive Index of Tuberculosis Samples (Mohammed et al., 2023)

Tuberculosis Samples	RI
Normal	1.351
Tb1	1.343
Tb 2	1.345
Tb 3	1.347
Tb 4	1.348

3. RESULTS AND DISCUSSION

3.1 Au Thickness Variations

The effect of Au thin film on CL is discussed in this section, as illustrated in Figure 2(b). The Au thickness was varied by 45 nm, 50 nm, and 55 nm. At the time, the analyte's RI was 1.31 RIU for all Au films. Resonance peaks at 590 nm were obtained at 45 nm Au thickness with CL 0.171681 dB/cm and 0.483223 dB/cm for x-polarized and y-polarized, respectively. Meanwhile, the resonance wavelength (RW) is 600 nm in a Au thickness of 50 nm, with CL 0.365273 dB/cm for y-polarized and 0.129841 dB/cm for x-polarized, respectively, The RW shifts 1000 nm in this range, and WR is 600 nm in the Au thickness of 55 nm, with CL of 0.098 dB/cm for x-polarized and 0.275458 dB/cm for y-polarized, respectively. The simulation result shows that the thicker the Au layer, the smaller CL is. This effect occurs theoretically due to large attenuation of the plasmonic material to of the CL sensor. In other words, longer wavelengths will also be produced due to the thicker Au layer. This is accordingly with the concept that the wavelength of light entering is directly proportional to the

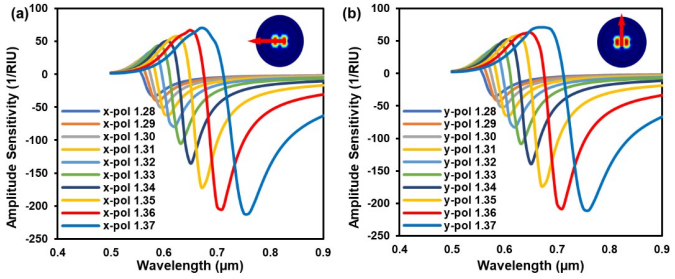

Figure 5. The Amplitude Sensitivity (AS) Plasmonic Sensor Component Was Investigated in Relation to the Variation of the RI From 1.28 RIU To 1.37 RIU. Under These Conditions, The Sensor Configuration Consisted of A Au Layer With A Thickness Of Dau = 50 Nm, A TiO_2 Layer With a Thickness Of $DTiO_2$ = 45 Nm, and A Perfectly Matched Layer (PML) With a Thickness Of 1 M. The AS Values Were Analyzed for Both X-Polarized (A) and Y-Polarized (B) Configurations As the RI of the Analyte Increased

depth of penetration of the sensor. These results also show similar values to those already reported by Yang et al. (2021) and Mahfuz et al. (2019).

3.2 Titanium Dioxide Thickness Variations

In this section the effect of TiO_2 or also known as the adhesive layer on sensor performance. TiO_2 layer is used to fix the adhesive problems experienced by Au thin films, although TiO_2 thin layer will not interfere with evanescent field penetration in the sample. it is proven that in this case the thickness variation of TiO_2 does not change the RW in Figure 2(a). The TiO_2 used in this sensor component has an optimized thickness of 50 nm. The CL sensor performance of each additional TiO_2 thickness is discussed. Variation of the thickness of TiO_2 at 40 nm, 45 nm and 50 nm, the refractive index of the analyte is set at 1.31 RIU. in Figure 2(a) The RW for each TiO_2 thickness is 600 nm, this adhesive layer can be used to reduce adhesive problems and also helps in bonding the Au thin film layer with fused silica material (Singh and Raghuwanshi, 2021) . The CL values obtained from 40 nm, 45 nm, and 50 nm TiO_2 were 0.1314 dB/cm (x-polarized) and 0.3676 dB/cm (y-polarized), 0.1304 dB/cm (x-polarized) and 0.3676 dB/cm (y-polarized), 0.1298 dB/cm (x-polarized) and 0.3653 dB/cm (y-polarized), respectively, while the resonance.

3.3 The Variations Thickness of a Perfectly Matched Layer

PML is the distribution limit of electromagnetic waves in the simulation, in this design the PML thickness is varied to determine its relationship with the confinement loss of the sensor, the thickness variations set in the design are 1 μm and 1.1 μm, x-polarized and y-polarized each are found to have a value consistent with the sensor design, in this PML thickness range it was found that CL has a value of 0.13 dB/cm (x-polarized) and 0.367 dB/cm (y-polarized) respectively, and 0.17 dB/cm (x-polarized) and 0.48 dB/cm (y-polarized), from these results the relationship is obtained that the thicker the PML indicates the greater the CL, so that a thickness of 1 μm in PML is an optimal and good value for the sensor. when viewed from the RW, a thickness of 1.1 μm has a RW of 590 nm while at a thickness of 1 μm the RW is found to be 600 nm, there is a 10 nm change for a thickness change of 0.1 μm, related to the thickness of PML to CL has also been previously considered by the researcher (Sarker and Faisal, 2023).

3.4 Hole Diameter Variations

The width of the air hole is an important parameter that influences signal loss on the sensor's surface. The greater the signal loss causes the increment of the air hole diameter. When the signal enters a large-diameter sensor component, the light energy will be pressed near the core to join SPP mode, as a result of this event will cause a high CL on the sensor component. The variations in diameter were set to be 1.45 μm, 1.50 μm, and 1.55 μm respectively. with CL at each air hole diameter of 0.13 dB/cm (x-polarized) and 0.75 dB/cm (y-polarized), 0.17 dB/cm (x-polarized) and 2.1 dB/cm (y-polarized), and 0.96 dB/cm (x-polarized) and 2.71 dB/cm (y-polarized). This set up produced that the greater the CL, the wider the air hole diameter, meanwhile the CL on y-pol is greater than CL on x-polarized. these results were confirmed by the the previous study which is reported by Shivam et al (S. Singh & Prajapati, 2020). Figure 2 shows the confinement loss peaks for changes in each physical parameter in the sensor design, 4(a) variations in Au thickness, 4(b) variations in air hole diameter, 4(c) variations in TiO_2 thickness, and 4(d) variations in PML thickness.

Meanwhile, Figure 3 describes the relationship between the SPP and the core for the analyte refractive index of 1.31 RIU, in this section the relationship between the x-polarized, y-polarized, real RI and SPP modes is introduced, the intersection of the graphs shows the high energy of the sensor , this interception point is also called the resonance condition which occurs at a wavelength of 750 nm with an analyte RI of 1.37 RIU, the wavelength range shown was yielded from 600 nm to 900 nm. Figure 3(a) is the electric field distribution around the sensor core with y-polarized, in this design it was found that y-polarized has good performance in the range of refractive index that can be detected by the sensor, Figure 3(b) is the distribution of the electric field at SPP mode, meanwhile Figure 3(c) is the distribution of the electric field at x-polarized, and Figure 3(d) is the relationship of x-polarized, y-polarized, real RI, and SPP mode on the sensor components. The maximum energy flow from the fundamental mode to the SPP mode is shown in Figure 3(b), the Au material was chosen in this work due to its chemical stability and also has a wide RW range, at an analyte refractive index of 1.37 RIU as well it is shown that the FWHM of the CL graph on y-polarized has a narrower value than on x-polarized. The CL curve of the sensor is determined using the imaginary value of the effective refractive index obtained from each x-polarized and y-polarized, this CL definitely becomes an important parameter, because

Table 3. Sensor Performance in Detecting the TB Bacteria

Sample	CL x-pol, y-pol (dB/cm)	RW (nm)	AS (1/RIU)	FWHM (nm)	FOM	Accuracy (1/nm)
Normal	0.703	670	-	40	-	0.025
	2.0085	670	-	40	-	0.025
Tb 1	0.5063	650	-103.1	30	66.67	0.033
	1.4479	650	-112.7	30	66.67	0.033
Tb 2	0.56	650	-24.04	35	-	0.028
	1.595	650	-24.45	35	-	0.028
Tb 3	0.59	660	-25.82	32.5	30.77	0.03
	1.68	660	-26.02	32.5	30.77	0.03
Tb 4	0.63	660	-12.22	43	-	0.023
	1.79	660	-12.23	43	-	0.023

the CL graph can be used as a parameter to find the resonant wavelength

3.5 Wavelength Sensitivity

The important analysis for measuring the sensitivity of the proposed sensor component is WS. It is known that the range of RI of the analyte that can be detected by the proposed sensor design is 1.27 RIU to 1.38 RIU and the RI of the analyte is 1.38 RIU with peaks at 950 nm and 920 nm for each x -pol and y-pol. Figure 4 depicts the shift in the confinement loss peak as well as the change in the analyte's RI on the x-axis polarization. The RW in this sensor design are varied of (560-950 nm) for x-polarized, whereas for y-polarized has a difference at the refractive index of 1.38 with the RW at 920 nm. So that this sensor design has a maximum WS for x-polarized and y-polarized of 20,000 nm/RIU and 17,000 nm/RIU, respectively. Further details for WS can be seen in Table 1. These results are better than previously reported by researchers for optical sensors that are applied in detecting normal cells and tuberculosis-infected cells. Like the component proposed by Ramanujam, the optical sensor only has a sensitivity of 700 nm/RIU (Ramanujam et al., 2020), sofyan et al proposed an optical sensor with a sensitivity of only 3197.18 nm/RIU (Taya et al., 2021), Arafa H aly proposed a sensor component with a sensitivity of 1390 nm/RIU in detecting normal cells and tuberculosis infected cells. Aly et al. (2021), and Parmar et al. (2022) with a proposed sensor component sensitivity of 1000 nm/RIU (Parmar et al., 2022). Meanwhile, the PCF-SPR component has a maximum WS of 20,000 nm/RIU and 17 nm/RIU at (x and y polarized).

3.6 Amplitude Sensitivity

AS is a very important parameter in SPR-based PCF sensors, in this sensor geometry AS can be seen in Figure 5 and it is obtained that consistent values for each (x and y-polarized) so that it can be used as a performance factor important in this optical sensor. AS is also defined as the difference between two confinement losses from two adjacent refractive index ranges. AS is highly dependent to the CL and on this sensor the refractive index range was obtained at 1.28 RIU to 1.37 RIU for AS., The smallest AS peak was occur at the refractive index of 1.28 RIU, while RI 1.37 has the largest AS peak. Respectively, AS peaks are at 580 nm and 760 nm, with AS values of -33.503 1/RIU and -211.38 1 /RIU. The AS peak shifts with the rise of the analyte RI as it can be seen for more details in Table 1. The AS peak for refractive index of 1.28 RIU at x-polarized and y-polarized is -33.503 and -35.3433 respectively. Furthermore, the AS peak is -42.715 1/RIU and -40.6 1/RIU respectively at y-polarized and x-polarized, at the analyte's RI of 1.29 RIU. Then, the analyte AS peak was -50.22 1/RIU and -51.6833 1/RIU respectively at x-polarized and y-polarized, at a RI of 1.29 RIU as it can be seen in Table 2. In this sensor design it was found that the peak of the AS on y-polarized has a value that tends to be greater than the peak of x-polarized, so that the energy distribution is greater on y-polarized than x-polarized.

3.7 Sensor Resolution and Accuracy

Sensor resolution (SR) is the sensor component that will appear in this work, This SR is calculated based on changes in refractive index and changes in minimum wavelength and changes in peak wavelength. Furthermore, the SR obtained from this sensor component is shown in Table 3, each range of refractive index has a different resolution, this difference is based on the CL distribution obtained from the refractive index of the analyte. In this design, the sensor resolution obtained is 9.17 × 10-5 RIU (x-polarized) and 1 × 10-4 RIU (y-polarized). Sensors accuracy will also provide a good value in sensing, sensor accuracy is obtained from the CL sensor graph and it is closely related to the width of the FWHM, the relationship shows that sensor accuracy is inversely proportional to the graph of FWHM for each CL of each analyte's refractive index, the narrower the FWHM indicates better sensor accuracy, in this design the SA for each analyte's refractive index is 1.27, 1.28, 1.29, 1.30, 1.31, 1.32, 1.33, 1.34, 1.35, 1.36, 1.37 each of 0.0167 /nm, 0.02 /nm, 0.025 /nm, 0.02/nm. 0.0143 /nm, 0.0133 /nm, 0.0125 /nm, 0.018 /nm, 0.0111 /nm, 0.0095 /nm and 0.0095. for the refractive index of 1.36 RIU and 1.37 RIU analytes have the same sensor accuracy because they have the same FWHM graph, meanwhile the accuracy in detecting a refractive index of 1.38 RIU cannot be found

because FWHM at this refractive index is not found. When compared to previous work, this sensor has a maximum SA of 0.025 /nm and shows more accurate results (Sarker and Faisal, 2023).

3.8 Performance of Sensor Detecting Tuberculosis

In this section, the sensor's performance in detecting tuberculosis is discussed using AS and CL, as shown in in Table 3. Especially in detecting normal and infected cells with tuberculosis type 1 the sensor has a WS of 2500 nm/RIU, these results are very promising and can be recommended for fabrication. Meanwhile the AS for each type of tuberculosis has significant differences as well as the CL value of each type tuberculosis. The CL peaks were 0.703 dB/cm (x-polarized) and 2.0085 dB/cm (y-polarized) in the normal cells, while the CL peaks for tuberculosis types 1, 2, 3, and 4 were 0.0563 dB/cm (x-polarized) and 1.4479 dB/cm (y-polarized), 0.56 dB/cm (x-polarized) and 1.595 dB/cm (y-polarized), 0.59 dB/cm (x-polarized) and 1.68 (y-polarized), 0.63 dB/cm (x-polarized) and 1.79 (y-polarized) respectively which can be seen in Table 3. CL spectra for each normal and infected analyte have the different FWHM characteristics, tuberculosis-indicated analytes have narrower FWHM than in normal analytes and except for tuberculosis-infected analyte type 4. Meanwhile, the resulting curation of each CL graph for each normal, infected Tb1, Tb2, Tb3, and Tb4 analyzer is 0.025 1/nm, 0.033 1/nm, 0.028 1/nm, 0.03 1/nm and 0.023 1/nm, as detailed in Table 3 .

Several non-optical components have been used as a tuberculosis diagnostic test tool, this technology has its own advantages and disadvantages, such as detection tools using the chest x-ray device, tuberculin skin test, and interferon-gamma release assays (Datta et al., 2019), The advantages possessed by the CXR device are low operating costs, having a portable form suitable for cells and allowing for computer-assisted sensing, but this device requires skilled staff to read the resulting data, for TST devices have advantages such as low-cost and easy-to-use devices. used, but this device takes a long time to diagnose the disease and the sensitivity of components can be reduced at any time. Positive used of TST result does not always indicate that mycobacterium tuberculosis is present in the patient's body. While the IGRAs component has advantages such as greater sensitivity compared to the previous components and only requires one clinical consultation for the patient, meanwhile it has disadvantages such as very high costs and requires laboratory resources in characterizing the components, from this explanation we have confidence that the PCF-SPR optical components has much better performance than existing components, as well as when compared to other optical components PCF-SPR is much more sensitive and profitable.

4. CONCLUSION

Tuberculosis which has killed many patients needs very early treatment, of course early diagnosis will save many patient lives, existing technology still has many weaknesses so that it requires alternative components that have good ability, high-sensitivity, fast and portable in responding to all problems. In this paper we conducted a numerical study of the combined components of PCF and SPR sensor technology in detecting the refractive index of normal and tuberculosis patients with types 1, 2, 3, and 4. In this design it was found that our sensor is able to detect tuberculosis infected cells with very high sensitivity as compared to the previously reported components, the sensor's WS was obtained at 20,000 nm/RIU (x-polarized) and 17,000 nm/RIU (y-polarized). Besides that the maximum AS was obtained at -211.38 1/RIU (x-polarized) and -211.211 1/RIU (y-polarized), while the sensor resolution, maximum FOM, minimum FWHM and AS were obtained 190.5 1/RIU, 40 nm, 0.025 1/nm respectively. This sensor has narrower than previous work and it can be applied in early detection of tuberculosis with very good ability.

5. ACKNOWLEDGMENT

We would like to thank LPPM Universitas Riau for their invaluable assistance in this research, which was funded by DRTPM Desentralisasi under contract number. 11309/UN19.5.1.3/AL .04/2023. We would also like to thank the head of the University of Riau's Optoelectronic Laboratory and the LPDP for the magister fellowship.

REFERENCES

Abdelghaffar, M., Y. Gamal, W. Soliman, Y. Badr, M. F. O. Hameed, and S. Obayya (2022). Early Cancer Detection by Plasmonic Pcf Sensor. *Proceedings of the International Conference on Numerical Simulation of Optoelectronic Devices*; 147–148

Aly, A. H., D. Mohamed, Z. Zaky, Z. Matar, N. Abd El-Gawaad, A. Shalaby, F. Tayeboun, and M. Mohaseb (2021). Novel Biosensor Detection of Tuberculosis Based on Photonic Band Gap Materials. *Materials Research*, **24**

Brixner, B. (1967). Refractive-index Interpolation for Fused Silica. *JOSA*, **57**(5); 674–676

Chen, W., C. Liu, X. Liu, Y. Feng, H. Liang, T. Shen, and W. Han (2023). Photonic Crystal Fiber Refractive Index Sensor Based on Spr. *Optical and Quantum Electronics*, **55**(2); 134

Datta, B., A. K. Prakash, D. Ford, P. K. Tanwar, P. Goyal, P. Chatterjee, S. Vipin, A. Jaiswal, N. Trehan, and K. Ayyagiri (2019). Comparison of Clinical and Cost-effectiveness of Two Strategies Using Mobile Digital X-ray to Detect Pulmonary Tuberculosis in Rural India. *BMC Public Health*, **19**; 1–8

Eid, M. M., A. N. Z. Rashed, A. A.-M. Bulbul, and E. Podder (2021). Mono-rectangular Core Photonic Crystal Fiber (mrc-pcf) for Skin and Blood Cancer Detection. *Plasmonics*, **16**; 717–727

Falah, A. A. S., W. R. Wong, and F. R. M. Adikan (2022). Single-mode Eccentric-core D-shaped Photonic Crystal Fiber Surface Plasmon Resonance Sensor. *Optics & Laser Technology*, **145**; 107474

Geneva (2023). *Strategic and Technical Advisory Group for Tuberculosis (STAG-TB): report of the 22nd meeting, Geneva, Switzerland, 6–8 June 2022*. World Health Organization

Gu, S., W. Sun, M. Li, Z. Li, X. Nan, Z. Feng, and M. Deng (2022). Simultaneous Measurement of Magnetic Field and Temperature Based on Photonic Crystal Fiber Plasmonic Sensor with Dual-polarized Modes. *Optik*, **259**; 169030

Han, B., Y. n. Zhang, E. Siyu, X. Wang, D. Yang, T. Wang, K. Lu, and F. Wang (2019). Simultaneous Measurement of Temperature and Strain Based on Dual Spr Effect in Pcf. *Optics & Laser Technology*, **113**; 46–51

Irawan, D., K. Ramadhan, and A. Azhar (2022a). Design of PCF-SPR for Early Detection of Skin Cancer Infected Cells. *Jurnal Penelitian Pendidikan IPA*, **8**(5); 2293–2298

Irawan, D., K. Ramadhan, F. Fitmawati, D. Hanto, and B. Widiyatmoko (2022b). High-performance of Starphotonics Crystal Fiber Based on Surface Plasmon Resonance Sensor. *Indian Journal of Pure & Applied Physics (IJPAP)*, **60**(9); 727–733

Irawan, D., K. Ramadhan, S. Saktioto, F. Fitmawati, D. Hanto, and B. Widiyatmoko (2022c). Hexagonal Two Layersphotonics Crystal Fiber Based on Surface Plasmon Resonance with Gold Coating Biosensor Easy to Fabricate. *Indonesian Journal of Electrical Engineering and Computer Science*, **28**(1); 146

Irawan, D., K. Ramadhan, S. Saktioto, and A. Marwin (2022d). Performance Comparison of Topas Chirped Fiber Bragg Grating Sensor with Tanh and Gaussian Apodization. *Indonesian Journal of Electrical Engineering and Computer Science*, **26**(3); 1477–1485

Jabin, M. A., K. Ahmed, M. J. Rana, B. K. Paul, M. Islam, D. Vigneswaran, and M. S. Uddin (2019). Surface Plasmon Resonance Based Titanium Coated Biosensor for Cancer Cell Detection. *IEEE Photonics Journal*, **11**(4); 1–10

Johnson, P. B. and R.-W. Christy (1972). Optical Constants of the Noble Metals. *Physical review B*, **6**(12); 4370

Kumar, A., P. Verma, and P. Jindal (2023). Surface Plasmon Resonance Sensor Based on Mxene Coated Pcf for Detecting the Cancer Cells with Machine Learning Approach. *Microelectronic Engineering*, **267**; 111897

Li, Z., W. Hou, J. Hong, C. Fan, Y. Wei, Z. Liu, X. Lei, Y. Qiao, O. P. Hasekamp, and G. Fu (2022). The Polarization Crossfire (pcf) Sensor Suite Focusing on Satellite Remote Sensing of Fine Particulate Matter Pm2. 5 from Space. *Journal of Quantitative Spectroscopy and Radiative Transfer*, **286**; 108217

Liu, Q., Z. Ma, Q. Wu, and W. Wang (2020). The Biochemical Sensor Based on Liquid-core Photonic Crystal Fiber Filled with Gold, Silver and Aluminum. *Optics & Laser Technology*, **130**; 106363

Mahfuz, M. A., M. A. Hossain, E. Haque, N. H. Hai, Y. Namihira, and F. Ahmed (2019). A Bimetallic-coated, Low Propagation Loss, Photonic Crystal Fiber Based Plasmonic Refractive Index Sensor. *Sensors*, **19**(17); 3794

Matsui, T., J. Zhou, K. Nakajima, and I. Sankawa (2005). Dispersion-flattened Photonic Crystal Fiber with Large Effective Area and Low Confinement Loss. *Journal of Lightwave Technology*, **23**(12); 4178–4183

Mohammed, N. A., O. E. Khedr, E. S. M. El Rabaie, and A. A. Khalaf (2023). High-Sensitivity Early Detection Biomedical Sensor for Tuberculosis With Low Losses in the Terahertz Regime Based on Photonic Crystal Fiber Technology. *Photonic Sensors*, **13**(2); 230202

Otupiri, R., E. K. Akowuah, and S. Haxha (2015). Multichannel SPR biosensor based on PCF for multi-analyte sensing applications. *Optics express*, **23**(12); 15716–15727

Pan, F., A. Zhang, H. Pan, and C. Cao (2022). High Sensitivity Surface Plasmon Resonance Sensor Based on D-shaped High Birefringence Photonic Crystal Fibre. *Journal of Modern Optics*, **69**(10); 575–582

Panda, A. and P. D. Pukhrambam (2022). Study of Metal-porous Gan-based 1d Photonic Crystal Tamm Plasmon Sensor for Detection of Fat Concentrations in Milk. *Lecture Notes in Electrical Engineering*; 415–425

Parmar, J., S. K. Patel, V. Katkar, and A. Natesan (2022). Graphene-based Refractive Index Sensor Using Machine Learning for Detection of Mycobacterium Tuberculosis Bacteria. *IEEE Transactions on NanoBioscience*, **22**(1); 92–98

Rahaman, M. E., M. B. Hossain, and H. S. Mondal (2022). Effect of Background Materials in Photonic Crystal Fiber Sensor. *Optical Review*; 1–6

Rahman, M. M., F. A. Mou, M. I. H. Bhuiyan, and M. R. Islam (2020). Photonic Crystal Fiber Based Terahertz Sensor for Cholesterol Detection in Human Blood and Liquid Foodstuffs. *Sensing and Bio-Sensing Research*, **29**; 100356

Ramanujam, N., S. K. Patel, N. M. Reddy, S. A. Taya, D. Vigneswaran, and M. M. Rajan (2020). One-dimensional Ring Mirror-defect Photonic Crystal for Detection of Mycobacterium Tuberculosis Bacteria. *Optik*, **219**; 165097

Ramola, A., A. Marwaha, and S. Singh (2021). Design and Investigation of a Dedicated Pcf Spr Biosensor for Cancer Exposure Employing External Sensing. *Applied Physics A*, **127**(9); 643

Rifat, A. A., G. A. Mahdiraji, R. Ahmed, D. M. Chow, Y. Sua, Y. Shee, and F. M. Adikan (2015). Copper-graphene-based Photonic Crystal Fiber Plasmonic Biosensor. *IEEE Photonics Journal*, **8**(1); 1–8

Sarker, H. and M. Faisal (2023). Surface Plasmon Resonance Sensor Using Photonic Crystal Fiber for Sucrose Detection. *Sensing and Bio-Sensing Research*, **39**; 100544

Sehmi, H., W. Langbein, and E. Muljarov (2017). Optimizing the Drude-lorentz Model for Material Permittivity: Method, Program, and Examples for Gold, Silver, and Copper. *Physical Review B*, **95**(11); 115444

Sellmeier (1871). Zur Erklärung Der Abnormen Farbenfolge Im Spectrum Einiger Substanzen. *Annalen der physik*, **219**(6); 272–282

Sen, S., M. Abdullah Al Shafi, A. S. Sikder, M. S. Hossain, and M. M. Azad (2021). Zeonex Based Decagonal Photonic Crystal Fiber (d-pcf) in the Terahertz (thz) Band for Chemical Sensing Applications. *Sensing and Bio-Sensing Research*,

31; 100393
Shakya, A. K. and S. Singh (2022). Design of novel Penta core PCF SPR RI sensor based on fusion of IMD and EMD techniques for analysis of water and transformer oil. *Measurement*, **188**; 110513
Singh, S. and Y. Prajapati (2020). TiO2/gold-graphene Hybrid Solid Core Spr Based Pcf Ri Sensor for Sensitivity Enhancement. *Optik*, **224**; 165525
Singh, Y. and S. K. Raghuwanshi (2021). Titanium Dioxide (TiO2) Coated Optical Fiber-based Spr Sensor in Near-infrared Region with Bimetallic Structure for Enhanced Sensitivity. *Optik*, **226**; 165842
Taya, S. A., M. G. Daher, I. Colak, and O. M. Ramahi (2021). Highly Sensitive Nano-sensor Based on a Binary Photonic Crystal for the Detection of Mycobacterium Tuberculosis Bacteria. *Journal of Materials Science: Materials in Electronics*, **32**; 28406–28416
Tosi, D., S. Poeggel, I. Iordachita, and E. Schena (2018). Fiber Optic Sensors for Biomedical Applications. *Opto-Mechanical Fiber Optic Sensors: Research, Technology, and Applications in Mechanical Sensing*; 301–333
Wu, Q.-l., Y. Zhao, Y.-n. Zhang, and Y. Yang (2021). Characteristics of a New Multi-channel Sensing Device Based on C-type Photonic Crystal Fibers. *Optics & Laser Technology*, **134**; 106622
Yan, X., Z. Guo, T. Cheng, and S. Li (2020). A Novel Gold-coated Pcf Polarization Filter Based on Surface Plasmon Resonance. *Optics & Laser Technology*, **126**; 106125
Yang, H., M. Liu, Y. Chen, L. Guo, G. Xiao, H. Liu, J. Li, and L. Yuan (2021). Highly Sensitive Graphene-au Coated Plasmon Resonance Pcf Sensor. *Sensors*, **21**(3); 818
Zaki, S. E., A. Mehaney, and A. H. Aly (2022). Novel Highly-sensitive Heavy Metals Sensor-based 1d Phononic Crystal for NiCl2 Detection. *Optical and Quantum Electronics*, **54**(12); 811

